Supplementary Information for:

Wintertime Arctic sea spray aerosol composition controlled by sea ice lead microbiology

Rachel M. Kirpes[1], Daniel Bonanno[2], Nathaniel W. May[1], Matthew Fraund[2], Anna J. Barget[1], Ryan C. Moffet[2], Andrew P. Ault*[1,3], Kerri A. Pratt*[1,4]

[1]Department of Chemistry, University of Michigan, Ann Arbor, Michigan, 48109
[2]Department of Chemistry, University of the Pacific, Stockton, California, 95211
[3]Department of Environmental Health Sciences, University of Michigan, Ann Arbor, Michigan, 48109
[4]Department of Earth & Environmental Sciences, University of Michigan, Ann Arbor, Michigan, 48109
[†]Present address: Sonoma Technology, Petaluma, California, 94954

*Corresponding authors: prattka@umich.edu and aulta@umich.edu

This file contains supplementary text, 5 tables, and 9 figures.

Ion Chromatography Analysis of Surface Snow

Surface (top 6 cm) snow samples were collected near the aerosol sampling site, on the tundra, at the beginning of each atmospheric particle sample period. Two surface snow (top 6 cm) samples were collected over first year sea ice (15 km from the sampling site, ~ 3 km from open leads; 20 cm snow depth) on February 27, 2014. Samples were double-bagged in Whirl-pak low-density polyethylene bags and kept frozen at -40 °C. Immediately prior to analysis by ion chromatography, samples were placed in a refrigerator at ~6 °C to melt. Snow melt water was sampled into 200 µL sample injection loops with 1 mL syringes equipped with 0.22 µM PVDF filters. The ICS-1100 and ICS-2100 ion chromatographs were each equipped with a guard column (ICS-1100: CG12A-5 µm (3 x 30 mm) IonPac; ICS-2100: AG18 4 mm (4 x 50 mm), Dionex), analytical column (ICS-1100: CS12A-5 µm (3 x 150 mm) IonPac; ICS-2100: AS18 4 mm (4 x 250 mm), IonPac), suppressor (ICS-110: CSRS 500 (4 mm), ICS-2100: AERS 500 (4 mm), Dionex), and a heated conductivity cell (DS6, Dionex). Methanesulfonic acid (20 mM) was used as eluent for the cation column, and a KOH gradient generated by an EGC III KOH system was used as eluent for the anion column. All samples were run in triplicate, with average values and standard deviations reported herein. Limits of detection for the measured inorganic ions were 2.35 µM (Na^+), 0.18 µM (NH_4^+), 0.15 µM (Ca^{2+}), 0.12 µM (Mg^{2+}), 0.087 µM (K^+), 0.94 µM (Cl^-), 0.25 µM (NO_2^-), 0.32 µM (SO_4^{2-}), 0.025 µM (Br^-), and 0.11 µM (NO_3^-).

Analysis of SSA Particles by Fluorescence Microscopy

Individual particles from January 26 and February 26 – 27 samples were analyzed with the same Raman instrument for fluorescence analysis. Fluorescence spectra were collected from 540 – 600 nm with 0.1 s acquisitions over a 50 x 50 µm area with 0.5 step size to create fluorescence intensity maps of individual particles.[1]

Comparison of SSA Particle Composition to Surface Snow and Frost Flower Composition

In addition to the comparison of SSA particle average elemental ratios and seawater ratios shown in Fig. 1b, CCSEM-EDX particle composition was also compared to ion mole ratios, determined by IC, for surface snow collected over both tundra and sea ice during the sampling study (Table S3). Comparisons were also made to blowing snow and frost flower composition, determined previously near Utqiaġvik,[2,3] as well as seawater ratios[4] (Table S3). Springtime blowing snow near Utqiaġvik, AK has been previously characterized by sulfate depletion, from mirabilite precipitation impacting brine migration through snow above sea ice, and magnesium enrichment compared to seawater.[3] Similarly, frost flowers are also characterized by sulfate depletion compared to seawater.[2]

Considering the Mg/Na, S/Na, Cl/Na, and Ca/Na mole ratios overall, the measured individual SSA particles lacked similarity to the measured sea ice surface snow composition during this study and previously measured frost flowers (Table S3). In particular, both the sub- and supermicron SSA were characterized by higher S/Na, lower Cl/Na, and higher Ca/Na mole ratios compared to the frost flowers (Table S3). This finding is consistent with recent work demonstrating that frost flowers are not a source of SSA.[6] The sea ice surface snow composition was only similar to the supermicron SSA Mg/Na and S/Na ratios, suggesting that blowing snow from the sea ice likely did not serve as a source for the measured SSA. Unlike tundra snow, sea ice snow is impacted by upward brine migration up to ~17 cm above the sea ice, as well as SSA deposition.[20] It should be noted that the individual SSA were statistically similar to previously measured blowing snow,[3] but this is due to the high variability in these previously reported values. Sea ice surface snow measured in this study was enriched in calcium, yet the measured Ca/Na mole ratio differed from the observed SSA. As described below, the sea ice surface snow enrichment in Ca,

compared to seawater, was likely due to influence of SSA deposition, as described below. The presence of mineral dust in snow could influence the Ca/Na ratio and would be expected to produce particles upon blowing snow sublimation, following the hypothesized process. However, as we reported previously,[21] individual mineral dust and fly ash particles comprised less than 1 %, by number, of the submicron particles during this elevated wind sampling period, and no supermicron dust was observed.

Overall, the measured individual SSA particles were closest in composition to seawater and tundra surface snow (Table S3). The similarity of tundra surface snow to the individual observed SSA, as well as seawater, is in part due to the high variability in the measured values, but it is also consistent with SSA deposition to the snowpack following transport from the upwind sea ice region containing leads. Further, submicron S/Na ratios were similar to seawater and tundra surface snow and did not show sulfate depletion expected for frost flowers or blowing snow,[2,3] or when compared to measured sea ice surface snow (Table S3). The supermicron SSA particles were depleted in sulfur compared to seawater and tundra surface snow composition, but not depleted to the levels previously observed for frost flowers.[2] The submicron SSA showed Mg and Ca enrichment above the seawater ratio; this is consistent with the presence of the observed presence of EPS as assembled gels bound by divalent cations (Ca^{2+}; Mg^{2+})[22,23] and as observed previously for mid-latitude SSA with EPS coatings.[23] It is also consistent with the greater C/Na ratios observed for the submicron SSA, compared to supermicron SSA (Figure 2); this size-dependence is also consistent with previous mid-latitude SSA studies.[23] Overall, measured individual SSA particle composition (elemental ratios, morphology, organic composition, size-dependent trends) followed that expected for SSA and did not consistently exhibit trends expected for blowing snow or frost flower sources for all elements or across size ranges. Surface snow composition above

tundra was consistent with SSA deposition, and sea ice surface snow composition was consistent with both upward brine migration and SSA deposition.

Previous work hypothesized a frost flower source for carbohydrate signatures detected in bulk winter – spring ambient aerosol samples at Utqiaġvik, AK under high wind and oceanic influence.[5] However, as noted above, more recent work has shown frost flowers do not fracture to produce aerosol.[6,7] In addition, our previous multiyear study examining sea salt aerosol (bulk aerosol IC measurements) as a function of wind speed and sea ice conditions showed supermicron SSA production during elevated wind speeds and lead/open water influence, and without the presence of fresh supermicron SSA when leads/open water were not present, consistent with a lead/open water-based SSA source, rather than blowing snow.[8] As described above, our individual SSA chemical composition results also support lead-based SSA production, rather than blowing snow or frost flower aerosol production.

Analysis of SSA Raman Spectra

Figure 4 shows Raman spectra of representative individual particles for each organic class, based on comparisons to standard spectra (Table S4). The standard model spectra within each organic type (e.g. all saccharides) were similar, exhibiting Raman peaks for the same functional groups; therefore, ambient SSA spectra are classified by general organic types (saccharides, short chain fatty acids, long chain fatty acids, amino acids). The ambient SSA particle spectrum representative of saccharides (arabinose, $\chi^2 = 0.01$) had characteristic peaks at 1014, 1050, and 1095 cm^{-1}, corresponding to ν(C-C) and ν(C-O) and a peak at 1127 cm^{-1} corresponding to ν_s(C-C).[9,10] A peak corresponding to $\delta(CH_2/CH_3)$ was observed at 1436 cm^{-1}.[11,12] $\nu_s(CH_3)$ and $\nu_a(CH_2)$ peaks were observed at 2906 and 2942 cm^{-1}, respectively.[11,13] ν(O-H) stretching peaks were observed at 3250 and 3410 cm^{-1}, likely due to particulate water (Fig. 4, Table S5).[11,13–15] The SSA

particle spectrum representative of short chain fatty acids (hydroxyhexanoic acid + butyric acid, χ^2 = 0.003) had peaks at 1062 and 1121 cm^{-1} corresponding to ν_a(C-C) and ν_s(C-C), 1297 and 1444 cm^{-1} for $\delta(CH_2)$ and $\delta(CH_3)$ peaks, and 2847, 2883, and 2910 cm^{-1} characteristic of $\nu_s(CH_2)$, $\nu_s(CH_3)$, and $\nu_a(CH_2)$, respectively, in addition to a ν(O-H) stretching peak at 3389 cm^{-1} (Fig. 4, Table S5).[10,11,13,16,17] The particle spectrum representative of long chain fatty acids (hydroxymyristic acid + oleic acid, χ^2 = 0.0005) had characteristic peaks at 1065 and 1130 cm^{-1} corresponding to ν_a(C-C) and ν_s(C-C and at 1296 cm^{-1} corresponding to $\delta(CH_2)$, in addition to $\delta(CH_2)$/ $\delta(CH_3)$ modes at 1444 cm^{-1}.[10–12] Peaks at 2844, 2880, and 2930 cm^{-1} correspond to $\nu_s(CH_2)$, $\nu_s(CH_3)$, and $\nu_a(CH_2)$, respectively (Fig. 4, Table S5).[11,13] The particle spectrum representative of amino acids and saccharides (lipopolysaccharide + bovine serum albumin, χ^2 = 0.016) had characteristic peaks at 858 cm^{-1} corresponding to ν(C-N-C) amino, ν_a(C-O-C) and ν(C-C) peaks at 996 and 1045 cm^{-1}, respectively, 1353 cm^{-1} for an amide III peak, 1455 cm^{-1} corresponding to $\delta(CH_3)$ and 1606 cm^{-1} for an amide I peak.[9,10,12] $\nu_s(CH_3)$ and $\nu_a(CH_2)$ peaks were observed at 2890 and 2938 cm^{-1}, respectively, in addition to a $\nu_a(CH_3)$ peak at 2976 cm^{-1} and ν(O-H) at 3391 cm^{-1} (Fig. 4, Table S5).[10,15,17,18] There was no detectable ν(N-H) peak in the spectrum representative of amino acids and saccharides, likely due to the low abundance of amino acids and the weak polarizability of N-H moieties making identification by Raman difficult.[19] A fraction of particle Raman spectra (19 %, by number) did not match any standard organic compounds due to fluorescence, burning, or low organic signal during Raman analysis (χ^2 value > 0.05 and/or spectral signatures of fluorescence/burning).

Organic Coating Thickness

Organic coating thicknesses for submicron and supermicron particles were determined using average organic volume fractions of 0.45 based on STXM-NEXAFS analysis. The median

aerodynamic diameter for the submicron (440 nm) and supermicron (1400 nm) particle size ranges collected were used to determine the total volume of a representative submicron and supermicron particle, assuming the particles (both core and shell) to be spherical. The inorganic volume was then determined, in order to calculate the organic coating thickness (difference between total volume and inorganic volume). A coating thickness of 9 %, or 130 nm for a supermicron (1400 nm d_a) particle and 40 nm for a submicron (440 nm d_a) particle, was determined for particles with 0.45 organic volume fractions.

Atomic force microscopy was used to measure the degree of spreading for the winter SSA and showed an average spreading ratio (height/radius) of 2.3 ± 0.6. However, both the inorganic and organic components spread similarly, with spreading ratios for just the inorganic cores averaging 2.7 ± 0.6. Estimating the coating thickness with AFM using these measurements gave similar results to the estimations using STXM-NEXAFS organic volume fraction data.

Table S1: Aerosol sampling timing and meteorological conditions measured at the NOAA Barrow Observatory.

Sample name/date	Sample Time (AKST)	Sampling duration (h)	Average wind speed (m s^{-1})	Wind speed range (m s^{-1})
January 24-25	10:16-10:02	24	12	8.6-14.9
January 26 day	11:00-17:15	6.25	8	6.2-9.9
January 27-28	10:55-10:30	23.5	6	3.9-8.1
February 26-27	19:45-8:30	12.5	10	5.8-16.6
February 27	8:50-19:30	10.5	12	8.5-15.3
February 27-28	20:00-7:20	11.25	10	6.9-15.0

Table S2: STXM-NEXAFS number fractions of individual SSA particles containing organics, as well as individual SSA particle organic volume fractions, for the four analyzed samples.

Sample timing (AKST) and aerodynamic diameter range	Number Fraction of SSA containing organics	Average SSA organic volume fraction	# of particles analyzed
Jan 26 11:00-17:15 (1.0-1.8 μm)	0.88±0.08	0.41±0.04	16
Jan 26 11:00-17:15 (0.32-0.56 μm)	1.00	0.5±0.1	13
Feb 26-27 19:45-8:30 (1.0-1.8 μm)	1.00	0.44±0.08	21
Feb 26-27 19:45-8:30 (0.32-0.56 μm)	0.98±0.01	0.4±0.2	103

Table S3: SSA particle composition and snow composition. Snow, frost flower, and seawater ion ratios and aerosol particle elemental ratios and 95 % confidence intervals.

Sample Type	Mg^{2+}/Na^{+} Or Mg/Na Mole Ratio	SO_4^{2+}/Na^{+} Or S/Na Mole Ratio	Cl^{-}/Na^{+} Or Cl/Na Mole Ratio	Ca^{2+}/Na^{+} Or Ca/Na Mole Ratio	Reference
Submicron SSA (average)	0.17 ± 0.02	0.05 ± 0.01	1.08 ± 0.03	0.085 ± 0.007	
Supermicron SSA (average)	0.12 ± 0.01	0.0330 ± 0.0006	1.19 ± 0.03	0.031 ± 0.004	
Seawater	0.11	0.06	1.16	0.022	Pilson[4]
Sea ice surface snow	0.12784 ± 0.00002	0.0360 ± 0.0001	1.223 ± 0.001	0.07030 ± 0.00004	
Tundra surface snow	0.13 ± 0.09	0.061 ± 0.05	1.1 ± 0.8	0.06 ± 0.05	
Frost flowers	0.135 ± 0.005	0.016 ± 0.003	1.30 ± 0.03	0.0216 ± .0009	Douglas et al.[2]
Blowing snow	0.2 ± 0.1	0.02 ± 0.01	1.2 ± 0.9	0.05 ± 0.03	Jacobi et al.[3]

Table S4: List of standard compounds available for matching in the Raman spectra reference library.[9]

Saccharides	Short chain fatty acids	Long chain fatty acids	Amino acids
Acetylnearuaminic acid	Adipic acid	Avanti Lipid A	Bovine Serum Albumin
Arabinose	Butyric acid	DPPA	Ethanolamine
Arabitol	Caproic acid	DPPC	Serine
Dextrin	Citric acid	Myristic acid	
Fucose	Malic acid	Hexadecanol	
Galactose	Decanoic acid	Hydroxymyristic acid	
Glucose	Docosanol	Lauric acid	
Inulin	Enanthic acid	Oleic acid	
Laminarin	Glutaric acid	Palmitic acid	
LPS	Hexanoic acid	Stearic acid	
Mannitol	Hydroxyhexanoic acid	Tridecanoic acid	
Rhamnose	Malonic acid	Triolein triglyceride	
Sialic acid	Nonanoic acid	Tripalmitin triglyceride	
Sucrose	Octanoic acid		
	Oxalic acid		
	Succinic acid		
	Valeric acid		

Table S5: Peak assignments for vibrational modes and associated intensities (strong (s), medium (m), weak (w)) observed in individual SSA particle Raman spectra.

Observed Peak	Peak Intensity	Raman Mode	Literature Peak Position	Reference
858	m	ν(CNC) amino	853	De Gelder et al.[10]
873, 877	m	δ(COH)	861	Cochran et al.[9]
927, 939	w			
996	m	ν_a(C-O-C)	991	Cochran et al.[9]
1014	w	ν(C-C), ν(C-O)	1009	Cochran et al.[9]
1045, 1050	s	ν(C-C)	1044	Cochran et al.[9]
1062, 1065	w	ν_a(C-C)	1063	De Gelder et al.[10]
1095	m	ν(C-O)	1095	De Gelder et al.[10]
1121, 1127, 1130	m	ν_s(C-C)	1128	De Gelder et al.[10]
1285	m			
1296, 1297	w	δ(CH_2)	1296	De Gelder et al.[10]
1323	w			
1353	w	Amide III	1351	De Gelder et al.[10]
1372	w			
1436, 1444	m	δ(CH_2)/δ(CH_3)	1440	Ault et al.[11] Mertes et al.[12]
1455	w	δ(CH_3)	1459	McLaughlin et al. (18) De Gelder et al.[10]
1601				
1606	w	Amide I	1596	De Gelder et al.[10]
2723, 2725, 2727	w	overtone	2723, 2724	Cochran et al.[9]
2844, 2847	s	ν_s(CH_2)	2850	Ault et al.[11] ; Deng et al.[13]

2880, 2883, 2890, 2906	s	$\nu_s(CH_3)$	2870	Ault et al.[11] ; Deng et al.[13]
2910, 2930, 2938, 2942	w	$\nu_a(CH_2)$	2930	Ault et al.[11] ; Deng et al.[13]
2976	m	$\nu_a(CH_3)$	2974	McLaughlin et al.[18]
2986	s	$\nu_a(CH_3)$	2986	Larkin[19]
3013	m	ν(=C-H)	3005	Czamara et al.[24]
3389, 3391	w	ν(O-H)	3402	Vargas Jentzsch et al.[17]
3410	s	ν(O-H)	3430	Xiao et al.[15]

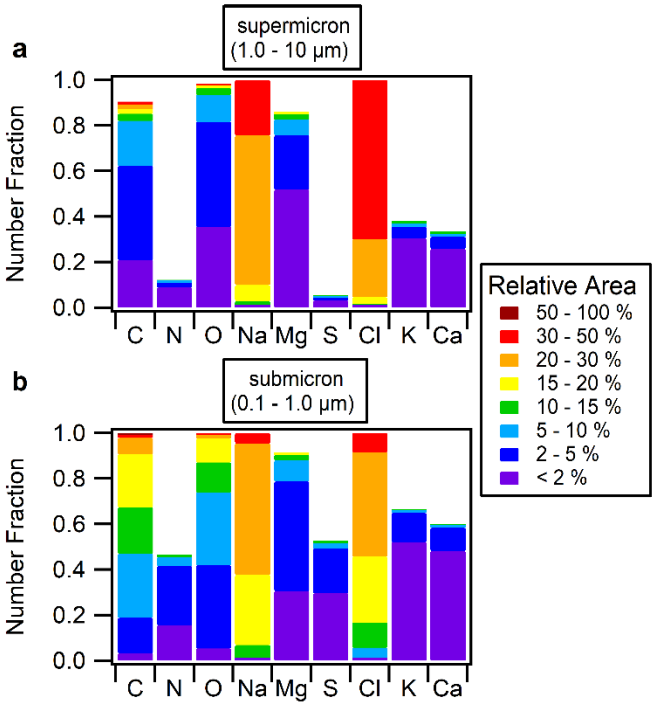

Figure S1: Digital color histograms showing the number fraction of spectra (particles) containing each element (bar height) at each EDX signal intensity range (color scale) for supermicron (a) and submicron (b) SSA particles. Al and Si are excluded due to interferences from sample holder and substrate, respectively.

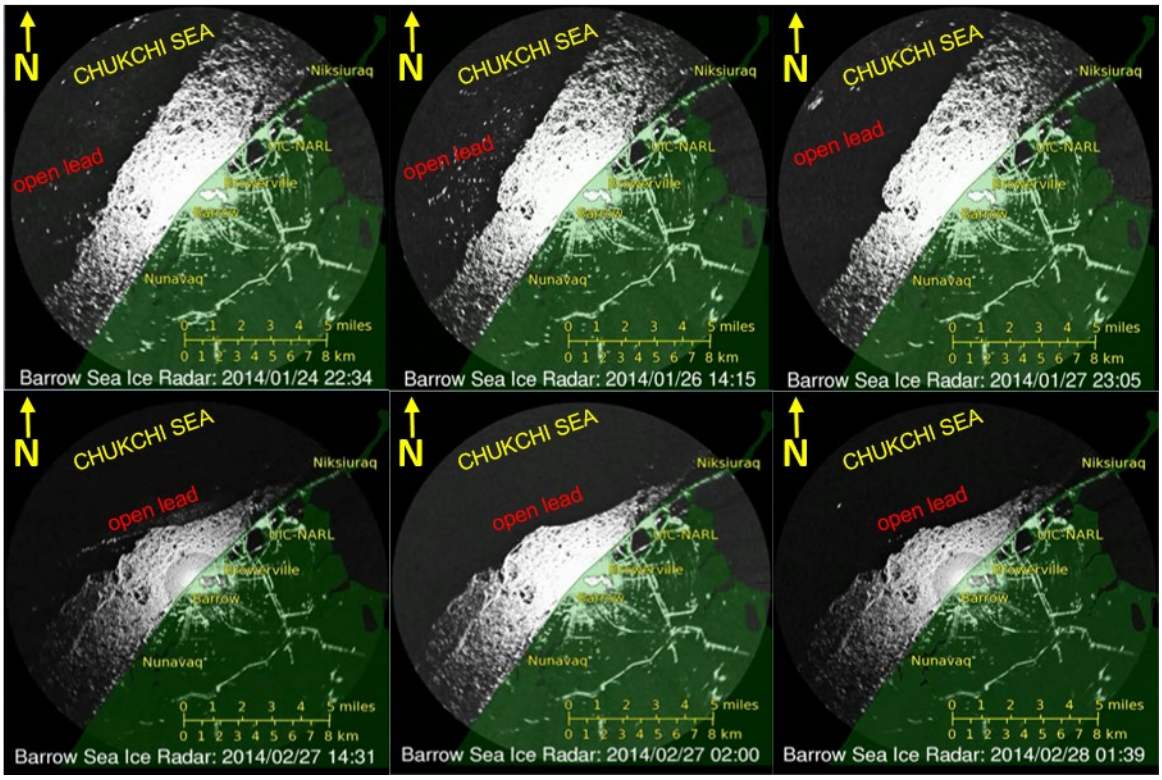

Figure S2: Representative Utqiaġvik (Barrow) coastal radar images showing the open lead present during each aerosol sampling period. The green region indicates land extent, and the white regions are sea ice. The lead was open for the duration of all samples. Images were obtained from the University of Alaska, Fairbanks Sea Ice group (http://seaice.alaska.edu/gi/data/barrow_radar).

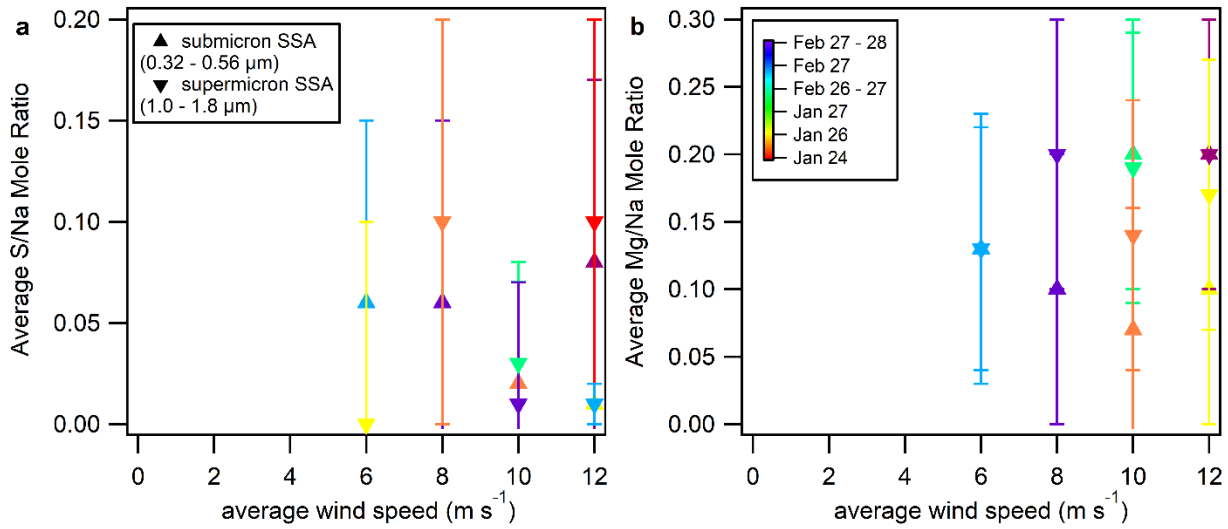

Figure S3: Average a) S/Na and b) Mg/Na mole ratios for submicron and supermicron SSA particles compared to wind speeds during each of the six winter sample periods. Error bars denote 95 % confidence intervals.

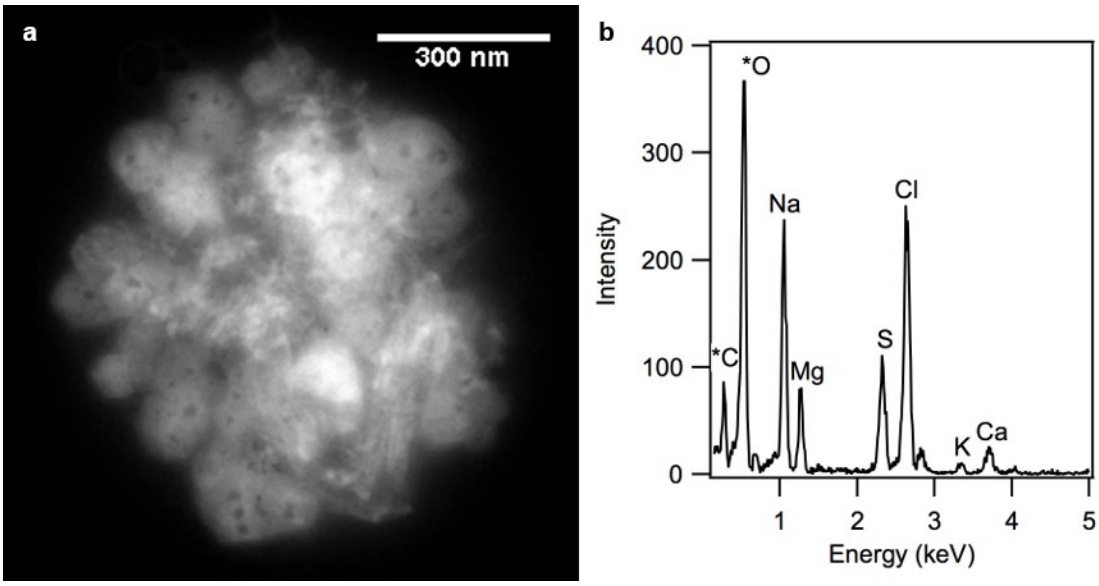

Figure S4: a) TEM image and b) EDX spectrum of a representative submicron wintertime SSA particle from January 26, containing both inorganic and organic components. *C and O signals include some influence from the TEM grid substrate film.

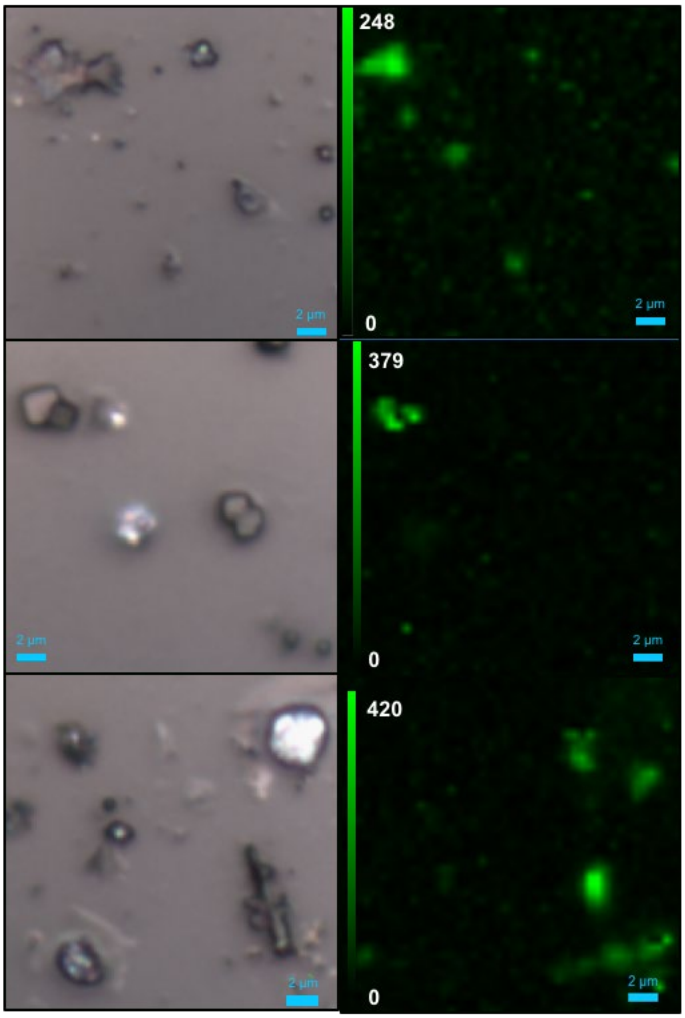

Figure S5: Representative optical images (left) and fluorescence maps (right), showing the fluorescence intensity counts (color scale) of individual SSA particles from February 26, 2014.

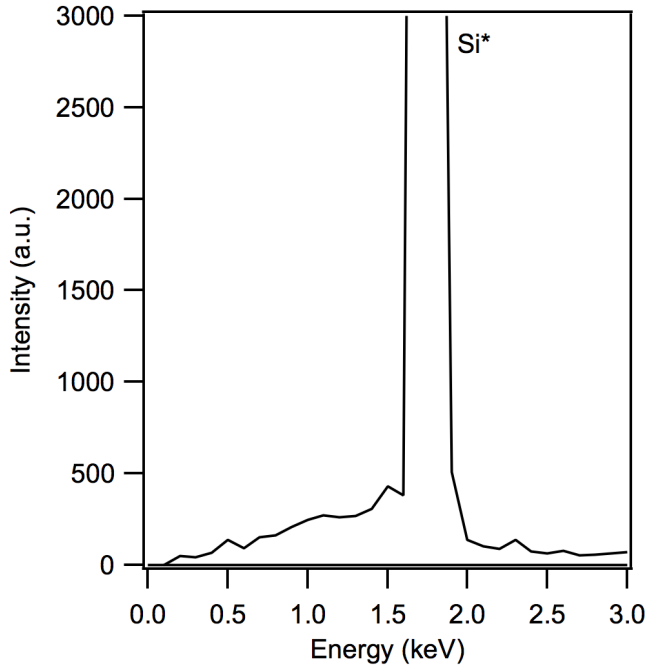

Figure S6: EDX spectrum of Si wafer background, showing no detectable contribution from carbon.

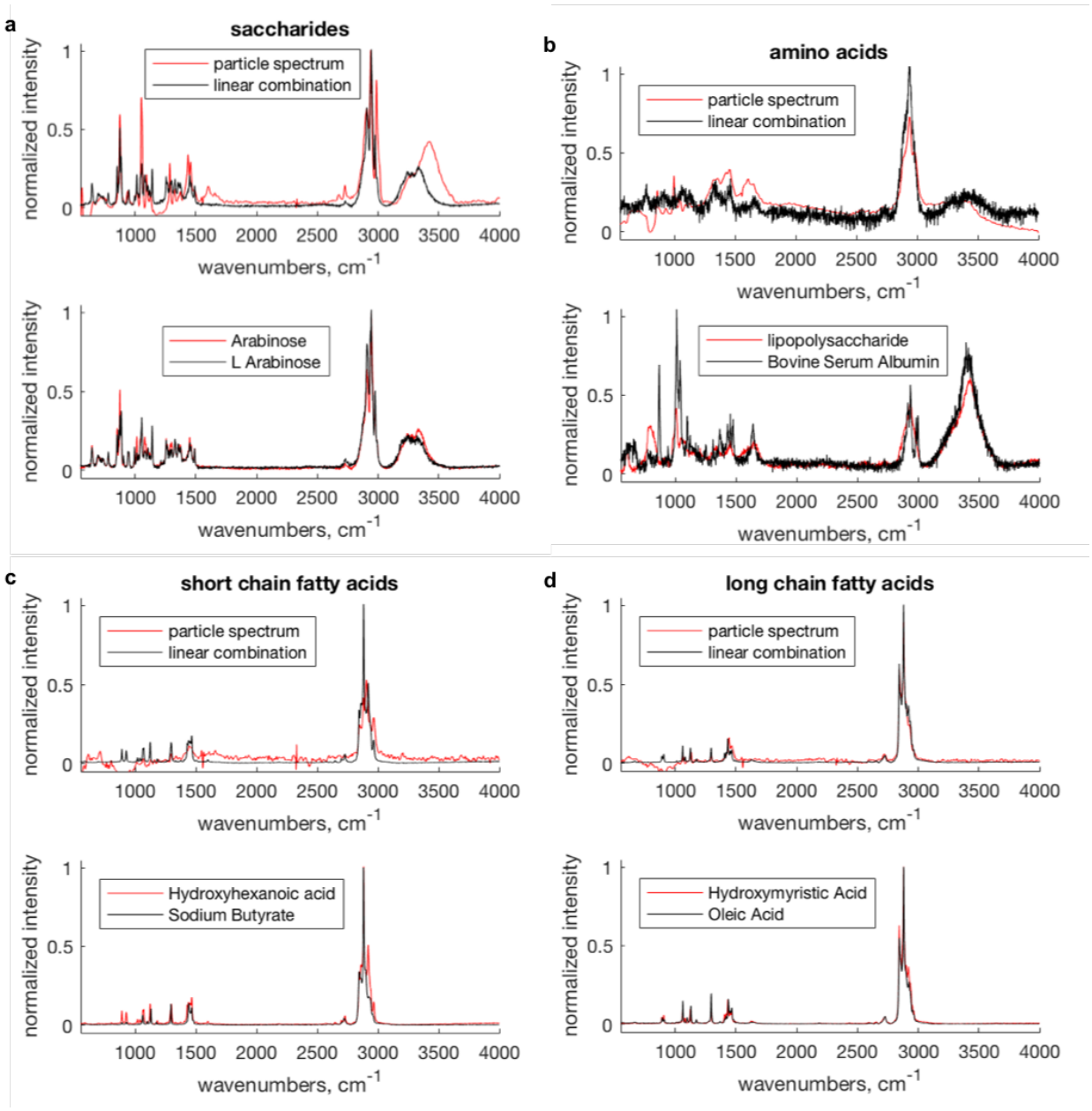

Figure S7: Linear combinations and χ^2 fits of representative SSA particle Raman spectra shown in Fig. 4 best matching a) saccharides, b) amino acids, c) short chain fatty acids, and d) long chain fatty acids.

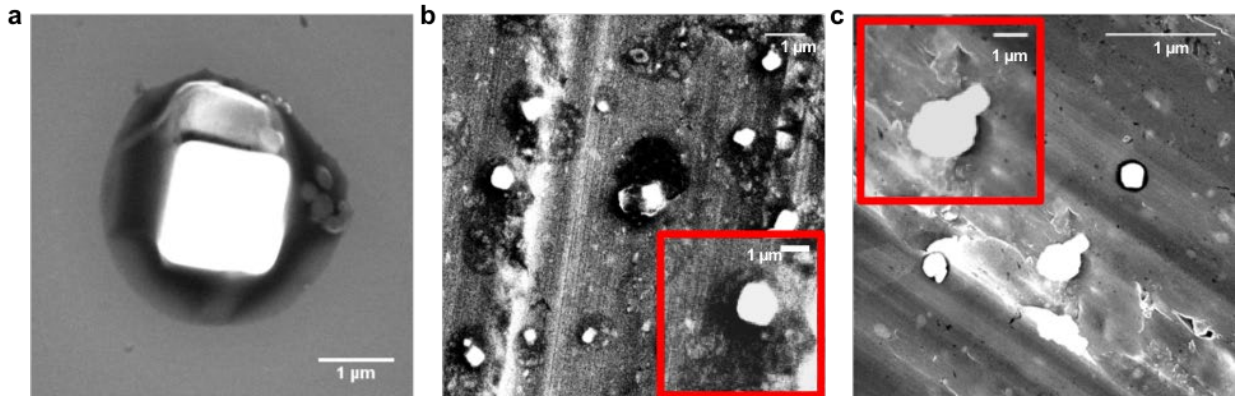

Figure S8: Representative SEM images of a) wintertime organic coated SSA particle on silicon, without outlines, and example b) wintertime, and c) summertime SSA particles on aluminum foil substrates, within insets highlighting representative particles.

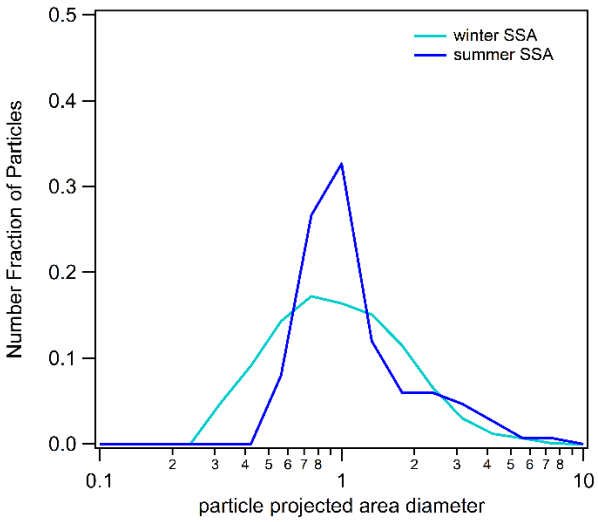

Figure S9: Size distributions for the individual particles analyzed by CCSEM-EDX to determine carbon to sodium ratios and organic coating to salt core ratios, for winter and summer SSA.

References:

1. May, N. W. et al. Aerosol Emissions from Great Lakes Harmful Algal Blooms. *Environmental Science and Technology* **2018**, *52* (2), 397–405. https://doi.org/10.1021/acs.est.7b03609.

2. Douglas, T. A. et al. Frost Flowers Growing in the Arctic Ocean-Atmosphere-Sea Ice-Snow Interface: 1. Chemical Composition. *Journal of Geophysical Research Atmospheres* **2012**, *117* (3), D00R09. https://doi.org/10.1029/2011JD016460.

3. Jacobi, H. W.; Voisin, D.; Jaffrezo, J. L.; Cozic, J.; Douglas, T. A. Chemical Composition of the Snowpack during the OASIS Spring Campaign 2009 at Barrow, Alaska. *Journal of Geophysical Research Atmospheres* **2012**, *117* (5), 1–13. https://doi.org/10.1029/2011JD016654.

4. Pilson, M. E. Q. *An Introduction to the Chemistry of the Sea*; Cambridge University Press, 2013; Vol. 51. https://doi.org/10.5860/choice.51-0291.

5. Shaw, P. M.; Russell, L. M.; Jefferson, A.; Quinn, P. K. Arctic Organic Aerosol Measurements Show Particles from Mixed Combustion in Spring Haze and from Frost Flowers in Winter. *Geophysical Research Letters* **2010**, *37* (10), L10803. https://doi.org/10.1029/2010GL042831.

6. Yang, X. et al. Evaporating Brine from Frost Flowers with Electron Microscopy and Implications for Atmospheric Chemistry and Sea-Salt Aerosol Formation. *Atmospheric Chemistry and Physics* **2017**, *17* (10), 6291–6303. https://doi.org/10.5194/acp-17-6291-2017.

7. Roscoe, H. K. et al. Frost Flowers in the Laboratory: Growth, Characteristics, Aerosol, and the Underlying Sea Ice. *Journal of Geophysical Research* **2011**, *116* (D12), D12301. https://doi.org/10.1029/2010JD015144.

8. May, N. W.; Quinn, P. K.; McNamara, S. M.; Pratt, K. A. Multiyear Study of the Dependence of Sea Salt Aerosol on Wind Speed and Sea Ice Conditions in the Coastal Arctic. *Journal of Geophysical Research* **2016**, *121* (15), 9208–9219. https://doi.org/10.1002/2016JD025273.

9. Cochran, R. E. et al. Molecular Diversity of Sea Spray Aerosol Particles: Impact of Ocean Biology on Particle Composition and Hygroscopicity. *Chem* **2017**, *2* (5), 655–667. https://doi.org/10.1016/j.chempr.2017.03.007.

10. De Gelder, J.; De Gussem, K.; Vandenabeele, P.; Moens, L. Reference Database of Raman Spectra of Biological Molecules. *Journal of Raman Spectroscopy* **2007**, *38* (9), 1133–1147. https://doi.org/10.1002/jrs.1734.

11. Ault, A. P. et al. Raman Microspectroscopy and Vibrational Sum Frequency Generation Spectroscopy as Probes of the Bulk and Surface Compositions of Size-Resolved Sea Spray Aerosol Particles. *Physical Chemistry Chemical Physics* **2013**, *15* (17), 6206–6214. https://doi.org/10.1039/c3cp43899f.

12. Mertes, S.; Dippel, B.; Schwarzenböck, A. Quantification of Graphitic Carbon in Atmospheric Aerosol Particles by Raman Spectroscopy and First Application for the Determination of Mass Absorption Efficiencies. *Journal of Aerosol Science* **2004**, *35* (3), 347–361. https://doi.org/10.1016/j.jaerosci.2003.10.002.

13. Deng, C.; Brooks, S. D.; Vidaurre, G.; Thornton, D. C. O. Using Raman Microspectroscopy to Determine Chemical Composition and Mixing State of Airborne Marine Aerosols over the Pacific Ocean. *Aerosol Science and Technology* **2014**, *48* (2), 193–206. https://doi.org/10.1080/02786826.2013.867297.

14. Frost, R. L.; Erickson, K. L.; Kloprogge, T. J. Vibrational Spectroscopic Study of the Nitrate Containing Hydrotalcite Mbobomkulite. *Spectrochimica Acta - Part A: Molecular and Biomolecular Spectroscopy* **2005**, *61* (13–14), 2919–2925. https://doi.org/10.1016/j.saa.2004.11.002.

15. Xiao, H. S. et al. Spatially Resolved Micro-Raman Observation on the Phase Separation of Effloresced Sea Salt Droplets. *Environmental Science and Technology* **2008**, *42* (23), 8698–8702. https://doi.org/10.1021/es801181f.

16. De Villepin, J.; Novak, A.; Bougeard, D. α- And β Phases of Oxalic Acid, H2C2O4: Vibrational Spectra, Normal-Coordinate Calculations, and Intermolecular Forces. *Chemical Physics* **1982**, *73* (3), 291–312. https://doi.org/10.1016/0301-0104(82)85170-7.

17. Jentzsch, P. V.; Kampe, B.; Ciobotă, V.; Rösch, P.; Popp, J. Inorganic Salts in Atmospheric Particulate Matter: Raman Spectroscopy as an Analytical Tool. *Spectrochimica Acta - Part A: Molecular and Biomolecular Spectroscopy* **2013**, *115*, 697–708. https://doi.org/10.1016/j.saa.2013.06.085.

18. McLaughlin, R. P.; Bird, B.; Reid, P. J. Vibrational Analysis of Isopropyl Nitrate and Isobutyl Nitrate. *Spectrochimica Acta - Part A Molecular and Biomolecular Spectroscopy* **2002**, *58* (12), 2571–2580. https://doi.org/10.1016/S1386-1425(02)00022-7.

19. Larkin, P. J. *Infrared and Raman Spectroscopy: Principles and Spectral Interpretation*, 1st ed.; Elsevier Science: Amsterdam, 2011.

20. Domine, F.; Sparapani, R.; Ianniello, A.; Beine, H. J. The Origin of Sea Salt in Snow on Arctic Sea Ice and in Coastal Regions. *Atmospheric Chemistry and Physics Discussions* **2004**, *4* (4), 4737–4776. https://doi.org/10.5194/acpd-4-4737-2004.

21. Kirpes, R. M. et al. Secondary Sulfate Is Internally Mixed with Sea Spray Aerosol and Organic Aerosol in the Winter Arctic. *Atmospheric Chemistry and Physics* **2018**, *18* (6), 3937–3949. https://doi.org/10.5194/acp-18-3937-2018.

22. Orellana, M. V.; Leck, C. Marine Microgels. *Biogeochemistry of Marine Dissolved Organic Matter: Second Edition* **2014**, *4*, 451–480. https://doi.org/10.1016/B978-0-12-405940-5.00009-1.

23. Jayarathne, T. et al. Enrichment of Saccharides and Divalent Cations in Sea Spray Aerosol during Two Phytoplankton Blooms. *Environmental Science and Technology* **2016**, *50*

(21), 11511–11520. https://doi.org/10.1021/acs.est.6b02988.

24. Czamara, K. et al. Raman Spectroscopy of Lipids: A Review. *Journal of Raman Spectroscopy* **2015**, *46* (1), 4–20. https://doi.org/10.1002/jrs.4607.